End-to-end simulator of two-dimensional interferometric radiometry

Ignasi Corbella,[1] Adriano Camps,[1] Miguel Zapata,[1] Fernando Marcos,[2]
Francisco Martínez,[3] Francesc Torres,[1] Mercè Vall-llossera,[1]
Nuria Duffo,[1] and Javier Bará[1]

Received 11 March 2002; revised 20 June 2002; accepted 20 June 2002; published 11 June 2003.

[1] An end-to-end simulator for the assessment of the performances of a spaceborne interferometric radiometer measuring the brightness temperature of Earth's surface (ground and sea) is presented. The tool covers the complete simulation of the input brightness temperature map, the full instrument modeling, the instrumental error correction, and the inversion algorithm to recover the brightness temperature. The output maps are presented in a graphical format including most of the standard cartographic projections. The simulator has been developed with two main objectives: (1) to provide the engineers a tool to predict system performance, and (2) to provide the scientific and end users a tool to help them in the implementation and improvement of algorithms for the Soil Moisture and Ocean Salinity (SMOS) retrieval for the SMOS Earth Explorer Opportunity Mission of the European Space Agency. *INDEX TERMS:* 6924 Radio Science: Interferometry; 6969 Radio Science: Remote sensing; 6974 Radio Science: Signal processing; 6982 Radio Science: Tomography and imaging; 6994 Radio Science: Instruments and techniques; *KEYWORDS:* interferometric aperture synthesis, microwave radiometry, SMOS mission, brightness temperature imaging, simulation tools

Citation: Corbella, I., A. Camps, M. Zapata, F. Marcos, F. Martínez, F. Torres, M. Vall-llossera, N. Duffo, and J. Bará, End-to-end simulator of two-dimensional interferometric radiometry, *Radio Sci.*, *38*(3), 8058, doi:10.1029/2002RS002665, 2003.

1. Introduction

[2] In recent years much attention has been paid to analyze the technological feasibility of L-band interferometric radiometers devoted to soil moisture (SM) and/or ocean salinity (OS) retrieval with acceptable spatial resolution. Such instruments produce brightness temperature images out of the measured cross-correlations between pairs of output signals measured by a large number of receivers. This technique is the core of MIRAS (Microwave Imaging Radiometer by Aperture Synthesis), the main payload of the ESA Earth Explorer Opportunity Mission SMOS, scheduled to be launched in 2006.

[3] To date, no full 2-D interferometric radiometer for Earth observation has been operated, and there are a number of specific details that have to be assessed to fully understand its capabilities and get insight into the way the output map is related to the geophysical parameters. In particular, the instrument images within a large field of view in which, among other instrument-related error sources, polarization mixing effects occur. This means that the instrument output has to undergo a significant amount of post-processing before getting a useful image. Additionally, improved emission models valid over a wide range of incidence angles have yet to be developed to take full advantage of the system. In this context, an end-to-end performance simulator becomes a very useful tool, and is of much help in the instrument design, the development of calibration and inversion techniques, and the test of geophysical parameter retrieval techniques using multiangle models, among others.

[4] This paper presents the SMOS end-to-end performance simulator developed under the frame of a specific contract within the project. It is an improved version of the software developed in the work of *Camps* [1996] and has the following capabilities: (1) satellite orbit simulation, (2) brightness temperature generator from available emission models, (3) accurate instrument modeling, (4)

[1]Department of Signal Theory and Communications, Universitat Politecnica de Catalunya, Barcelona, Spain.
[2]EADS-CASA Espacio, Madrid, Spain.
[3]EADS-CASA GMV S.A., Madrid, Spain.

0048-6604/03/2002RS002665$11.00

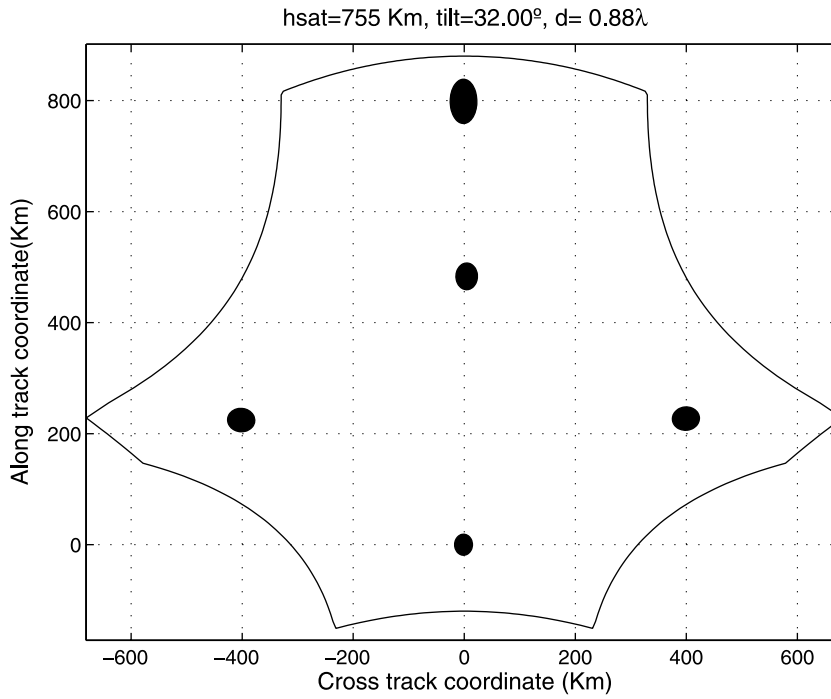

Figure 1. Instantaneous field of view of the instrument, showing also the pixel size and shape at different locations and the constant incidence angle contours.

internal calibration by noise injection, (5) inversion algorithm, (6) graphical output, maps, projections, etc., (7) system performance evaluation (spatial resolution, radiometric sensitivity, field of view over the Earth surface or in direction cosines, and geometrical issues (incidence angle, pixel shape, etc.)), and (8) friendly user interface.

[5] The integration of the new tool and the user interface have been developed by GMV S.A (Spain). The tool is written in open code platform independent Matlab© 5.3 and the computation time ranges between 15 and 20 min in a Pentium III at 1.2 GHz with 512 Mbytes of RAM.

2. The SMOS Mission and MIRAS, Its Payload Instrument

[6] The ESA's SMOS mission is aimed at retrieving Soil Moisture and Ocean Salinity at a global scale using L-band radiometry. The main mission requirements are (more information at http://www.cesbio.ups-tlse.fr/indexsmos.html and in the work of *Silvestrin et al.* [2001]: (1) global sea surface salinity maps (0.1 psu parameter resolution, 200 km spatial resolution, 7 days temporal resolution), (2) global Soil Moisture And Vegetation water content maps (0.035 m^3/m^3 and 0.2 kg/m^2 parameter resolution, 60 km spatial resolution, 3 days temporal resolution), and (3) cryosphere: improved assessment of snow mantle and multilayered ice structure.

[7] The interferometric radiometer of the mission is an array of antennae in a Y-shaped structure [*Martín-Neira and Goutoule*, 1997]. Each arm is about 4 m long and has 21 equally spaced receivers. In the center there are 9 extra antennae for calibration and redundancy purposes, so the total number of receivers is 72 ($= 21 \times 3 + 9$). The instrument will fly at a Sun-synchronous polar orbit with the local time ascending node set at 6.00 AM at an altitude of 755 km, and having the instrument boresight tilted 32° with respect to nadir. In these conditions, the instantaneous field of view (FOV) spans over a very large area, and is shown schematically in Figure 1. Inside the FOV each pixel has an elliptical shape (also shown in the figure) with different spatial resolution and radiometric accuracy in each one. Moreover, each pixel is measured at two orthogonal polarizations forming a different angle with respect to the standard horizontal and vertical ones. While the instrument is passing over a given zone, every pixel is measured a number of times, allowing to improve the radiometric resolution by averaging the series of independent measurements. A whole two-dimensional (2-D) brightness temperature image is generated every basic integration time, limited to 0.3 s owing to hardware requirements. Each one is indepen-

dent from the precedent and subsequent ones, so no orbital maneuvers such as yaw steering are required.

3. Satellite Orbit Simulation

[8] The spacecraft motion is simulated taking into account the relevant environmental conditions such as perturbation forces, spacecraft layout and initial orbital parameters. To compute the satellite position and the pixels being imaged at each snapshot an Earth-centered Earth-fixed (ECEF) system is selected. Satellite ephemeredes are computed by numerical integrating the Tesseral and Zonal harmonics up to order 18 and taking into account that at each step the platform's longitude has to be decreased according to the Earth rotation rate. For simplicity, the location of the platform is considered fixed during the integration time, so image blurring due to platform movement is not modeled.

4. Brightness Temperature Generator

[9] The brightness temperature generator is based on the one described in the work of *Camps et al.* [1998c]. It computes vertical and horizontal brightness temperatures by using the general equations available in the work of *Ulaby et al.* [1982], and taking into account the following physical parameters: soil and snow albedos, snow depth, soil roughness, vegetation albedos, soil moisture, soil surface temperature, ocean salinity, zonal and meridional winds over the oceans, vegetation height, ocean surface temperature and ocean ice cover for Earth and sea surfaces. The atmosphere upwelling, downwelling and attenuation are computed using a first-order approximation of Liebe's model for a standard atmosphere [*Liebe*, 1989], including rain intensity and water vapor concentration maps. Most of these parameters have been extracted from the CD set of [*Meeson et al.*, 1995; *Sellers et al.*, 1995], which is mapped with a spatial resolution of $1^\circ \times 1^\circ$ (110×110 km over the equator), larger than the instrument pixel over Earth's surface. To overcome this problem the resulting brightness temperature pixels are bilinearly interpolated to a thinner $1/12^\circ \times 1/12^\circ = 9.26$ km $\times$ 9.26 km grid and masked by the NOAA ETOPO5 5 min resolution global digital elevation model available at http://www.ngdc.noaa.gov/mgg/global/seltopo.html. This technique preserves the high-frequency contents given by the coast line.

[10] The brightness temperature at the antenna frame is converted to local Earth coordinates using the appropriate coordinate conversion:

$$\begin{bmatrix} E_v \\ E_h \end{bmatrix}^{ant} = \bar{A}\bar{P}\bar{F} \begin{bmatrix} E_v \\ E_h \end{bmatrix}^{pix}, \tag{1}$$

where $\bar{A}$, $\bar{P}$ and $\bar{F}$ are 2×2 matrices that model the errors introduced by the antennae, the change in the polarization base and the Faraday rotation respectively. Third and fourth Stokes parameters are not computed because the instrument is not polarimetric. Sun and moon presence in the field of view of the instrument as well as Sky noise, both directly captured by the instrument and reflected over Earth are also included as options selected by the user.

5. Instrument Modeling

5.1. Basic Equations

[11] Operation of a 2-D interferometric radiometer is based on the integral relationship existing between the brightness temperature map of an extended source as a function of the direction cosines $T_B(\xi, \eta)$ and the so-called visibility function $V(u, v)$, obtained from the complex cross-correlation measured between the output signals of all pairs of antennae [*Ruf et al.*, 1988]. In particular, if $b_1(t)$ and $b_2(t)$ are the output analytic signals of two given receivers, the visibility function is conveniently defined as:

$$V(u,v) = \frac{1}{k\sqrt{B_1 B_2}\sqrt{G_1 G_2}} \frac{1}{2} \left\langle b_1(t) b_2^*(t) \right\rangle, \tag{2}$$

where B_i and G_i are respectively the noise bandwidth and the available power gain of the receiver i ($i = 1, 2$) and k is the Boltzmann constant. The symbols $\langle\rangle$ stand for infinite time average, limited in practice to the integration time. The spatial coordinates u and v are defined as $u = \Delta x/\lambda$ and $v = \Delta y/\lambda$ being Δx and Δy the projections over the x and y axis of the vector going from one antenna to the other and λ the wavelength at the center frequency of measurement. Using this definition, the relation between the visibility and the brightness temperature is given by:

$$V(u,v) = \int\int_{\xi^2+\eta^2<1} T'(\xi,\eta)\tilde{r}\left(-\frac{u\xi + v\eta}{f_0}\right) \cdot e^{-j2\pi(u\xi+v\eta)} d\xi d\eta, \tag{3}$$

where ξ and η are the direction cosines referred to the same coordinate system as u and v, and $T'(\xi, \eta)$ is the so-called modified brightness temperature defined as

$$T'(\xi,\eta) = \frac{T_B(\xi,\eta)}{\sqrt{1-\xi^2-\eta^2}} \frac{F_1(\xi,\eta)F_2^*(\xi,\eta)}{\sqrt{\Omega_1\Omega_2}}, \tag{4}$$

being $F_i(\xi, \eta)$ and Ω_i the normalized complex voltage pattern and solid angle respectively of antenna i ($i = 1, 2$). The function $\tilde{r}(\tau)$ in equation (3) is called the fringe

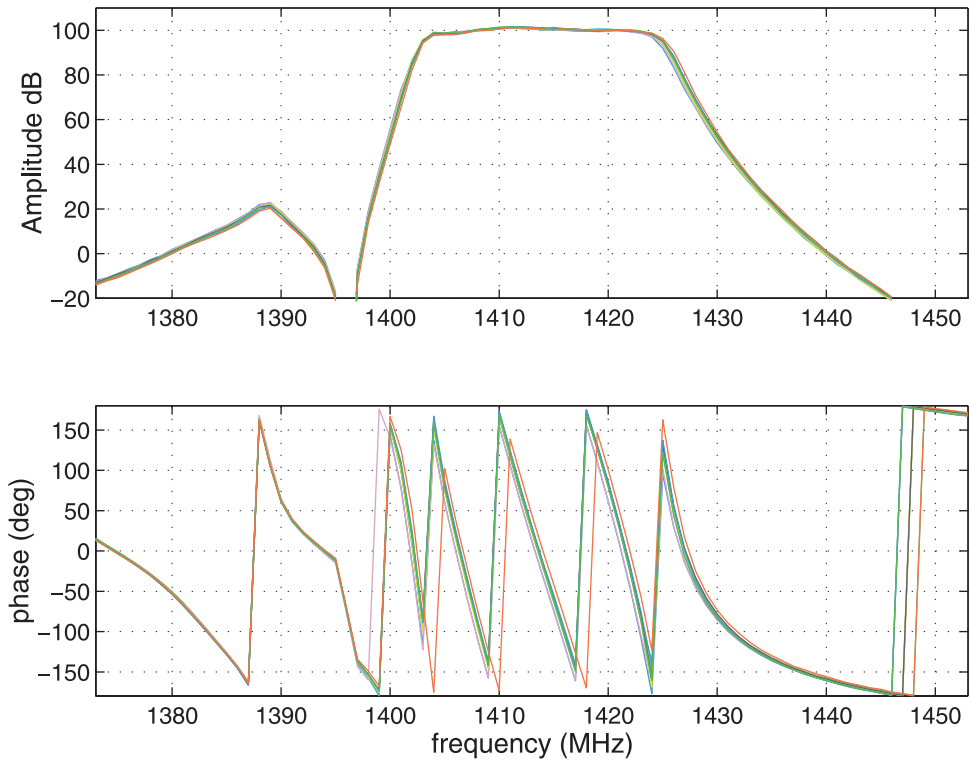

Figure 2. Frequency response of 10 receivers as computed by the simulator.

washing function and depends on the complex frequency response of the receivers. In particular, for band-pass receivers its amplitude has a sinc-like shape being almost unity at the origin, and its phase can be approximated by an order 2 polynomial. For identical receivers and antennae and narrow field of view (i.e., $\tilde{r}(\tau) \simeq 1$), equation (3) is a two-dimensional Fourier transform.

5.2. Antennae

[12] Each of the 72 individual antennae in the array is described by its normalized complex voltage pattern $F_i(\xi, \eta)$, its ohmic efficiency and its input matching, being these two last parameters used in the receivers frequency response computation module. Since the image is synthetically formed, the main beam efficiency of a particular antenna is not a key parameter, so it is not modeled.

[13] Two antenna pattern models have been implemented: (1) a list of measurements for different cuts, provided by the manufacturer (EADS-Casa Space division, Madrid, Spain), and (2) mathematical description using a formula $F(\theta) = \cos^n(\theta)$, where the parameter n is user selectable. In the second case, a pointing error of the antenna radiation maximum in the direction, and amplitude and phase error ripples in the antenna voltage pattern are also modeled. All antennae have dual polarization.

5.3. Receivers

[14] The receivers include a front-end with a polarization switch, a low-noise amplifier and an RF filter; a phase/quadrature mixer and duplicate IF sections for the in-phase and quadrature paths. The frequency response is shaped by the RF filter and covers the reserved band 1400–1427 MHz, although the cutoff frequencies are designed at 1404 and 1423 MHz to avoid interference from adjacent channels. The simulator computes the overall frequency response by cascading the individual parameters (i.e., S-parameters) of each subsystem (amplifiers, filters, mixers, ..). To this end, every subsystem is characterized by a nominal set of properly defined parameters, their tolerance and their temperature coefficient. With this information, and using a Gaussian random number generator, a different temperature-dependent frequency response for each receiver is computed. Figure 2 shows a plot of 10 frequency responses $H(f)$ computed as indicated. It can be seen that the shape is mainly governed by the RF filter and the high

attenuation in the lower part of the band is due to the rejection of the IF filter.

[15] The output IF signals (in-phase and quadrature) are sampled using a synchronous clock, then converted to 1-bit digital signals and sent to a matrix of 1-bit 2-level digital correlators to perform correlations between all pairs. When this kind of correlators are used the basic measurement is actually the normalized cross-correlation, defined as:

$$\mu = \frac{V}{\sqrt{T_{A1} + T_{R1}}\sqrt{T_{A2} + T_{R2}}}, \tag{5}$$

where T_{Ai} and T_{Ri} are respectively the antenna and receivers' noise temperature of receiver i (i = 1, 2) and V is the visibility function defined in (2). The simulator computes all the normalized cross-correlations using (5) and equation (3) and then adds a Gaussian random signal to emulate the thermal noise owing to finite integration time [*Camps et al.*, 1998b]. Offset and other effects introduced by the correlators errors are also taken into account using *Camps et al.* [1997c]. The mechanical oscillations of the arms are also modeled using the equations derived in the work of *Camps* [1996].

6. Calibration (Error Correction)

[16] Since an interferometric radiometer measures a complete map of brightness temperature in a single snapshot, a complete calibration should include measurement of known scenes. At present this point is still open, and until the availability of the actual instrument, only the simulator can be used as a tool for developing calibration schemes.

[17] Independently of the above it is advantageous to estimate most of the instrumental errors by an error correction procedure on the basis of noise injection. This is referred most times as internal calibration and it is thoroughly described in the work of *Torres et al.* [1996] and *Corbella et al.* [1998]. It is based on injecting to sets of receivers the noise that is generated by diodes and that is distributed through the appropriate passive networks. Normalized cross-correlations of receivers' output signals are computed as explained in the work of *Corbella et al.* [2000]. The noise-injection networks are simulated by computing the individual S-parameters of each 1:n power splitters and cascading the connecting transmission line, including losses and tolerance of dimensions and characteristic impedances.

[18] The internal calibration is a procedure to measure the fringe washing function at the origin ($\tilde{r}(0)$) and the receivers noise temperature T_{Ri}, this one used to compute the amplitude terms of (5). The shape of the fringe washing function is measured using time delays in the receivers while injecting correlated noise [*Camps et al.*, 1999], and this is also simulated by the tool.

7. Image Reconstruction

[19] Once the calibration has been carried out, the brightness temperature map is computed by inversion of equation (3) where now the fringe washing function is known and the antenna patterns and solid angles are assumed to have been measured with the needed accuracy to achieve the required radiometric performance [*Camps et al.*, 1997b].

[20] The first-order solution for the inversion of equation (3) is an inverse Fourier transform followed by a compensation of the average antenna pattern and the obliquity factor. Owing to the Y-shape of the instrument, the visibility sampling grid is hexagonal, so an hexagonal Fast Fourier Transform is used [*Camps et al.*, 1997a]. From this first-order solution, the inversion process continues in an iterative technique similar to the "CLEAN" algorithm, but suitably modified for extended sources [*Camps et al.*, 1998a]. Each iteration of the algorithm computes equation (3), including the measured fringe washing functions and individual antenna patterns.

[21] In order to avoid conditions that can not be met in a real situation, some "a priori" information is used in the inversion process, in particular, the Sky brightness temperature map, including the cosmic and galactic noises, the Sun and the moon. With this data, the differential visibility is defined as follows:

$$\Delta V(u,v) = V(u,v) - T_{SKY}V_{SKY}(u,v) - T_{EARTH}V_{EARTH}(u,v), \tag{6}$$

where $V_{SKY}(u, v)$ and $V_{EARTH}(u, v)$, computed with the same equation (3), are the contributions from the Sky, and for a uniform brightness temperature over Earth. T_{EARTH} is an average brightness temperature computed to force $\Delta V(0, 0) = 0$. The inversion algorithm described above is applied to this differential visibility, which makes the process much faster and robust.

[22] Figure 3 shows the original and recovered brightness temperatures in the direction cosines domain. Figure 3a shows the original temperature in the whole space ($\xi^2 + \eta^2 \leq 1$) and in Figure 3b the same temperature restricted to the instrument field of view. In Figure 3c, there is the recovered brightness temperature for the "ideal case," that is assuming identical receivers and no fringe-washing effects, thus leading to a simple Fourier transform relation. It is shown for comparison, since it represents the very best results that can be achieved with this concept. The errors between this map and the original one (top right) are due solely to the discretization and finite UV coverage of the data.

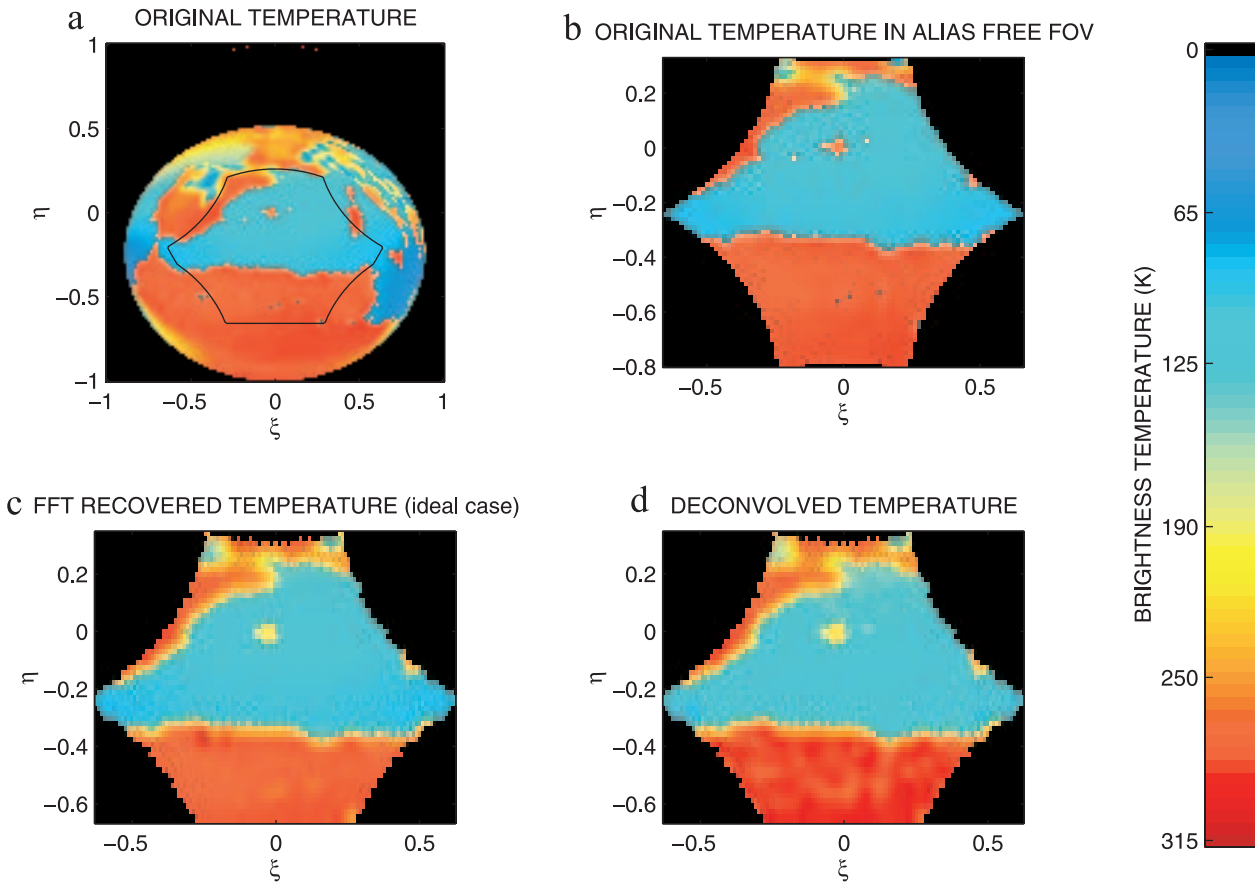

Figure 3. Brightness temperature maps in the direction cosines domain. (a) Original, as computed by the brightness temperature generator. (b) The same restricted to the instrument FOV. (c) The one that would recover an "ideal" system. (d) Recovered by a "real" system after calibration and inversion.

Finally, in Figure 4d there is the recovered brightness temperature map after computing the visibility including antenna and receiver errors, calibrating for estimation of these errors and inverted for getting the final map. As can be seen, the recovered brightness temperature is close to the ideal one, thus validating the algorithms used. The RMS error between these two last maps is less than 5 K with an integration time of 0.3 s.

8. Output Data Files and Graphical Representation

[23] Simulation results are saved in text files, ready to be used by an end user for further analysis. The available data include, for each pixel, its coordinates (latitude, longitude and director cosines), and all the computed dual polarization brightness temperatures, namely (1) theoretical (see section 4) horizontal and vertical, (2) retrieved by the instrument at antenna reference frame, and (3) retrieved by the instrument converted to horizontal and vertical over the ground. In the last case, some information is lost owing to the singularity of the rotation matrix around 45° when the third and fourth Stokes parameters are not available. However, since the lost pixels are different at each snapshot, the information can be recovered by postprocessing. Multi incidence angle analysis can also be performed by selecting individual pixels for a number of snapshots. This makes the simulator a powerful tool for tuning the corresponding algorithms. Other relevant information, such as platform position, orientation and velocity is also available. Details concerning the output data format is explained in the software user manual (reference SPS-UPC-70100-UMA-002).

[24] The software has also a powerful graphical representation capability. The original brightness temperature distribution, as well as the simulation results can be

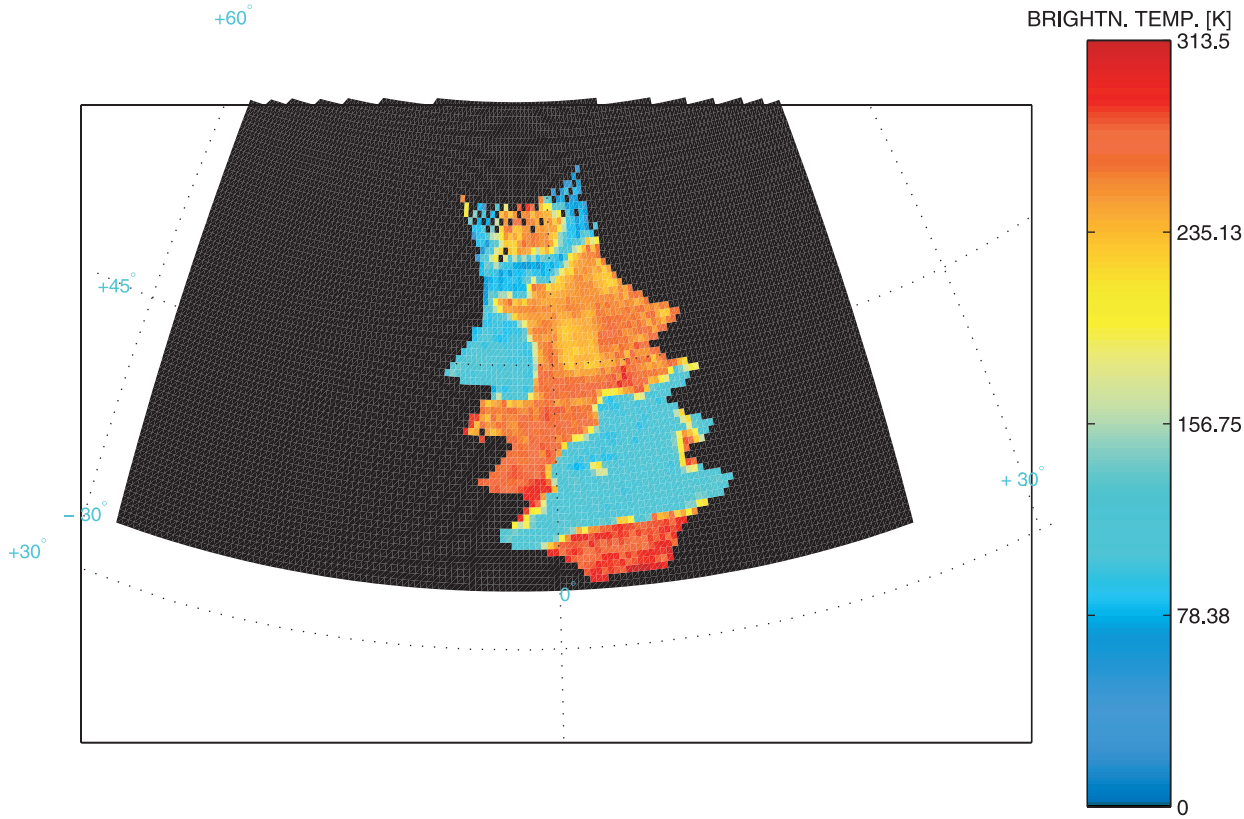

Figure 4. Brightness temperature after four snapshots projected over Earth.

displayed in the direction cosines representation and also in the cartographic projections and expansions listed as follows.

[25] 1. Cartographic projections: gnomonic (central, meridian and horizontal), stereographic (polar, meridian and horizontal), orthographic (equatorial, meridian and horizontal).

[26] 2. Cartographic expansions: Lambert's equivalent cylindrical expansion, equivalent cylindrical expansion with automecoic meridians, Mercator shaped cylindrical expansion, transverse cylindrical expansion, UTM projection, conical expansion, Lambert's shaped conical expansion. Figure 4 shows the recovered brightness temperature after 4 consecutive snapshots as a function of latitude and longitude using oblique orthographic projection.

9. Conclusions

[27] A complete end-to-end performance simulator of a two-dimensional interferometric radiometer has been presented. The tool is being used in the development of the instrument for the ESA mission SMOS and it is based on the research carried out by Universitat Politècnica de Catalunya during the past decade in connection with this project. It is a complete and operational tool providing realistic data to assess engineers in the instrument design as well to scientists in the development of retrieval techniques for geophysical parameters, and has also been useful for understanding the fundamentals of this technique. From the results obtained it becomes apparent that 2-D interferometry is a valid concept for Earth imaging radiometry, while at the same time its fundamental limitations are pointed out. These are, for example: poor radiometric sensitivity and accuracy in a single snapshot, large error near the alias-free FOV border, error amplification and singularities in the translation to pixel reference frame, high impact of receiver and antenna errors in the overall instrument performance, and unknown calibration methods.

[28] **Acknowledgments.** The SMOS End-to-End Performance Simulator has been developed with the financial support of (a) the Spanish Government under grants TIC 96/0879 and TIC1999-1050-C03-01 to UPC, and (b) the European Space Agency under contracts SEPA (ESTEC contract 14629/00/NL/SF) and SEPS (ESTEC contract 14907/00/NL/SF), acting in both cases EADS-Casa Division Espacio (Madrid-Spain) as main contractor.

References

Camps, A., Application of interferometric radiometry to earth observation, Ph.D. thesis, Univ. Politècnica de Catalunya, Catalunya, Spain, 1996.

Camps, A., J. Bará, I. Corbella, and F. Torres, The processing of hexagonally sampled signals with standard rectangular techniques: Application to 2-D large aperture synthesis interferometric radiometers, *IEEE Trans. Geosci. Remote Sens.*, *GRS-35*, 183–190, 1997a.

Camps, A., J. Bará, F. Torres, I. Corbella, and J. Romeu, Impact of antenna errors on the radiometric accuracy of large aperture synthesis radiometers: Study applied to MIRAS, *Radio Sci.*, *32*, 657–668, 1997b.

Camps, A., F. Torres, I. Corbella, J. Bará, and J. A. Lluch, Threshold and timing errors of 1 bit/2 level digital correlators in earth observation synthetic aperture radiometry, *Electron. Lett.*, *33*, 812–814, 1997c.

Camps, A., J. Bará, F. Torres, and I. Corbella, Extension of the CLEAN technique to the microwave imaging of continuous thermal sources by means of aperture synthesis radiometers, *in Prog. Electromagn. Res.*, *18*, 67–83, 1998a.

Camps, A., J. Bará, F. Torres, I. Corbella, and F. Monzón, Experimental validation of radiometric sensitivity in correlation radiometers, *Electron. Lett.*, *34*, 2377–2378, 1998b.

Camps, A., F. Torres, I. Corbella, J. Bará, and A. Abad, Modeling the radiometric signatures of the Earth from space: A tool to study the performance of new radiometers, in *The European Symposium on Aerospace Remote Sensing, Conference on Sensors, Systems and Next Generation Satellites IV*, pp. 787–795, Inst. Electr. Eng., London, 1998c.

Camps, A., F. Torres, I. Corbella, J. Bará, and F. Monzón, Automatic calibration of channels frequency response in interferometric radiometers, *Electron. Lett.*, *35*, 115–116, 1999.

Corbella, I., F. Torres, A. Camps, and J. Bará, A new calibration technique for interferometric radiometers, in *The European Symposium on Aerospace Remote Sensing, Conference on Sensors, Systems and Next Generation Satellites IV*, pp. 359–366, Inst. Electr. Eng., London, 1998.

Corbella, I., A. Camps, F. Torres, and J. Bará, Analysis of noise injection networks for interferometric radiometer calibration, *IEEE Trans. Microw. Theory Tech.*, *48*, 545–552, 2000.

Liebe, H. J., MPM—An atmospheric millimeter wave propagation model, *Int. J. Infrared Millimeter Waves*, *10*(6), 631–650, 1989.

Martín-Neira, M., and J. M. Goutoule, A two-dimensional aperture-synthesis radiometer for soil moisture and ocean salinity observations, *ESA Bull.*, *92*, 95–104, 1997.

Meeson, B. W., F. E. Corprew, J. McManus, D. Myers, K. S. J. W. Closs, D. Sunday, and P. J. Sellers, *ISLSCP Initiative I-Global Data Sets for Land-Atmosphere Models 1987–1988* [CD-ROM], NASA, Greenbelt, Md., 1995.

Ruf, C. S., C. T. Swift, A. B. Tanner, and D. M. Levine, Interferometric synthetic aperture microwave radiometry for the remote sensing of the Earth, *IEEE Trans. Geosci. Remote Sens.*, *26*, 597–611, 1988.

Sellers, P., et al., *An Overview of the ISLSCP Initiative I-Global Data Sets* [CD-ROM], NASA, Greenbelt, Md., 1995.

Silvestrin, P., M. Berger, Y. Kerr, and J. Font, ESA's second earth explorer opportunity mission: The Soil Moisture And Ocean Salinity Mission-SMOS, *IEEE Geosci. Remote Sens. Newslett.*, *188*, 11–14, 2001.

Torres, F., A. Camps, J. Bará, I. Corbella, and R. Ferrero, On-board phase and modulus calibration of large aperture synthesis radiometers: Study applied to MIRAS, *IEEE Trans. Geosci. Remote Sens.*, *GRS-34*, 1000–1009, 1996.

Ulaby, F. T., R. K. Moore, and A. K. Fung, *Microwave Remote Sensing: Active and Passive*, vol. II, *Radar Remote Sensing and Surface Scattering and Emission Theory*, Artech House, Norwood, Mass., 1982.

J. Bará, A. Camps, I. Corbella, N. Duffo, F. Torres, M. Vall-llossera, and M. Zapata, Department of Signal Theory and Communications, Universitat Politecnica de Catalunya, Campus Nord UPC, edifici D3, E-08034 Barcelona, Spain. (bara@tsc.upc.es; camps@tsc.upc.es; corbella@tsc.upc.es; duffo@tsc.upc.es; xtorres@tsc.upc.es; merce@tsc.upc.es)

F. Marcos, EADS-CASA, Space Division, ETS/Engineering Technology Systems, Av. Aragon 404, E-28022 Madrid, Spain. (fmarcos@casa-de.es)

F. Martínez, EADS-CASA GMV S.A., c/Isaac Newton 11, PTM Tres Cantos, E-28760 Madrid, Spain. (fmartinez@gmv.es)